Microsystem Technologies (2018) 24:3019–3032
https://doi.org/10.1007/s00542-017-3684-2

TECHNICAL PAPER

A low loss and power efficient micro-electro-thermally actuated RF MEMS switch for low power and low loss applications

Parviz Zolfaghari[1] · Vahid Arzhang[2] · Mojtaba Zolfaghari[3]

Received: 31 October 2017 / Accepted: 18 December 2017 / Published online: 6 January 2018

Abstract
A novel laterally and micro-electro-thermally actuated RF MEMS switch is presented in this paper. Despite many RF MEMS switches requiring continuous actuation voltage to hold the switch at ON-state, the proposed switch remains ON without any DC power. The mechanical design of the switch is in such a way that, the contact force of the switch is in mN range with zero DC power consumption. The switch is modeled and its operation is comprehensively analyzed. The fabrication process is completely compatible with standard MetalMUMPs process. The switch requires actuation voltages of 0.5 and 0.9 V for U-shaped and V-shaped actuators, respectively. The switch is normally OFF with isolation of − 20 dB up to 100 GHz. The insertion loss of the switch at ON-state is better than − 0.1 dB up to 40 GHz and the return loss is below − 10 dB up to 100 GHz. The power consumption of the switch is confined to the transition time of the switch between OFF and ON states. Based on analytical and numerical simulations, the contact resistance of the switch is 0.028 Ω. The proposed switch in this paper is dedicated for applications in mobile front-ends especially antenna switch networks where the signal loss and power consumption are the main constraints.

1 Introduction

Owing to many advantages of miniaturization, integration and enhanced performance, microelectromechanical systems (MEMS) technology have been increasingly employed in many applications including microfluidics (Bian et al. 2017; Vafaie et al. 2013; Ivanoff et al. 2016; Jain et al. 2017; Li et al. 2017a; Mirzajani et al. 2016; Yıldırım 2017), biosensors (Jayanthi et al. 2016; Lakshmipriya et al. 2017; Mirzajani et al. 2017b; Okyay et al. 2017; Takalkar et al. 2017; Wang et al. 2017), photonics (Atashzaban et al. 2013a, b; Lu et al. 2017; Nouet and Michel 2017; Trigona et al. 2016; Xu et al. 2017), Radio Frequency systems (Barzegar et al. 2015; Mirzajani et al. 2017c; Bonthu and Sharma 2017; Ilkhechi et al. 2016a, 2017; Kahmen and Schumacher 2017; Ilkhechi et al. 2016b; Kumar and Singh 2017; Li et al. 2017b; Liu et al. 2017; Lucibello et al. 2017; Mirzajani et al. 2015, 2017a; Song and Gong 2017) and *etcetera* (Demaghsi et al. 2012; Cheng et al. 2015; Tingkai et al. 2015; Demaghsi et al. 2014a; Demaghsi et al. 2014b). MEMS technology has made meaningful contribution into RF systems, especially, switches dedicated for low-loss and low-power applications (Rebeiz et al. 2009, 2013). Compared to semiconductor switches, RF MEMS switches have advantages in terms of lower loss and enhanced linearity especially at higher frequencies (higher than 10 GHz) (Daneshmand and Mansour 2011). Most of the RF MEMS switch performance depends on actuation mechanism (Rebeiz 2004). Three well-known methods for RF MEMS switch actuation are piezoelectric (Proie et al. 2012), electrostatic (He et al. 2012), and electro-thermal (Daneshmand et al. 2009). The application of piezoelectric actuators are very limited because of material unavailability and problems with CMOS compatibility (Pirmoradi et al. 2015; Xiang and Shi 2009). The electrostatic actuators are well-known for their near-zero power consumption (Chan et al. 2009). However, they require very high actuation voltages in the

✉ Parviz Zolfaghari
zolfaghari8parviz@gmail.com

Vahid Arzhang
Arzhang.vahid@gmail.com

Mojtaba Zolfaghari
Zolfaghari.mojtaba1@gmail.com

[1] Microelectronics Research Lab, Electrical Engineering Department, Sahand University of Technology, Tabriz, Iran

[2] Electrical Engineering Department, Amirkabir University of Technology, Tehran, Iran

[3] Department of Electrical Engineering, Islamic Azad University South of Tehran Branch, Tehran, Iran

range of around 100 V (Rebeiz 2004). On-chip generation of such a high voltage by voltage up-converters is both challenging and power consuming (voltage up-convertors consume a power of around 50–200 μW) (Rebeiz et al. 2009, 2013). Moreover, they suffer stiction (Muldavin et al. 2012; Sterner et al. 2011), dielectric charging problems, handle relatively lower RF power (Patel and Rebeiz 2012) and suffer from self-actuation. In contrast, electro-thermal actuators work with lower actuation voltages, produce high contact forces (leading to lower insertion loss), their fabrication process is completely CMOS compatible, use thicker layers than electrostatic switches and this makes them less sensitive respect to thermal conditions and mechanical vibrations and noises imposed from surrounding environment and has the potential to handle higher RF power with no self-actuation (Bakri-Kassem and Mansour 2015). The main problem is that, they consume a lot of power while the switch remains ON. In literature, mechanical latching technique is employed in order to decrease their power consumption (Daneshmand et al. 2009). However, by the use of latching technique which power in OFF, the contact force of the switch considerable decreases leading to increased contact resistance and insertion loss (Driesen et al. 2010).

Based on the new structure developed here, the latching mechanism is designed in such a way that, the switch consumes no DC power at the ON-state, yet the contact force is high (mN range), leading to lower contact resistance. Standard MetalMUMPs process is adopted for switch dimensional design (Cowen et al. 2002). The required actuation voltages of the switch are 0.5 and 0.9 V for U-shaped and V-shaped actuators, respectively. The initial gap between switch and transmission line in OFF-state is selected to be 20 μm. This large air gap considerably increases switch isolation up to terahertz frequencies. The presented switch is dedicated for applications where low actuation voltage, low power consumption, low insertion loss and high isolation are sought after.

2 Structure and operation

2.1 Switch structure

A 3-D schematic view of the proposed switch is shown in Fig. 1. The witch is integrated inside of a coplanar waveguide (CPW) transmission line (T-line) and is composed of three parts of L-shaped T-line, U-shaped microelectro-thermal actuators and V-shaped microelectro-thermal actuator. The L-shaped T-lines are suspended over the substrate and are anchored at their narrow end. They are designed in a tapered manner to have a narrow end in order to easily deflect in X-axes orientation by the aid of U-shaped actuators. The L-shaped T-lines are connected to the U-shaped microelectro-thermal actuators through a Si_3N_4 layer which serve as mechanical support and prevents RF signal leakage from L-shaped T-line to U-shaped actuators. The U-shaped microelectro-thermal actuators are used in the switch structure in order to pull back the L-shaped T-lines. They have two hot arms in order to effectively produce desired deflection with minimum power consumption and thermal distribution over the structure. The V-shaped microelectro-thermal actuator is used in order to make the switch ON or OFF. The actuator is connected to switching tip through Si_3N_4 layer. This layer serves as mechanical support and prevents RF signal leakage. Because the travelling range of the V-shaped actuator is high, a trench is created in substrate underneath the actuator beams in order to decrease heat leakage to substrate (Bakri-Kassem and Mansour 2015). Design procedure and dimensions of V-shaped and U-shaped actuators are provided in Sect. 3. Required actuation voltage of the V-shaped and U-shaped actuators are provided with meandered bias lines as shown in Fig. 2.

2.2 Switch operation

The switch operation is based on sequentially application of actuation voltage to U- and V-shaped actuators. The operation mechanism of the switch is divided to latching (switch becomes ON) and unlatching (switch becomes OFF) process.

2.2.1 Latching process (switch becomes ON)

The process of latching is schematically shown in Fig. 3 and is outlined here. As shown in Fig. 3a, at the beginning, the switching tip is away from the L-shaped T-lines and the switch is OFF. Figure 3b, in order to open the way of the switching tip, the U-shaped actuators are actuated to pull the L-shaped T-lines backward. Figure 3c, the V-shaped actuator is actuated in order to push the switching tip forward. Figure 3d, when the switching tip passed L-shaped T-lines, the U-shaped actuators become OFF and L-shaped T-lines come back to their rest position. Figure 3e, finally, the V-shaped actuator becomes OFF and switching tip stymie to the L-shaped T-lines and the switch becomes ON. The interesting thing about the design is that, when the switch is ON, all the actuators are OFF (U-shaped and V-shaped actuators) and the V-shaped actuator did not come back to its rest position and has a 30 μm residual deflection respect to its rest position. Because the restoring force of the V-shaped actuator is high, the contact force between L-shaped T-line and the switching tip is in mN range leading to a very low contact resistance.

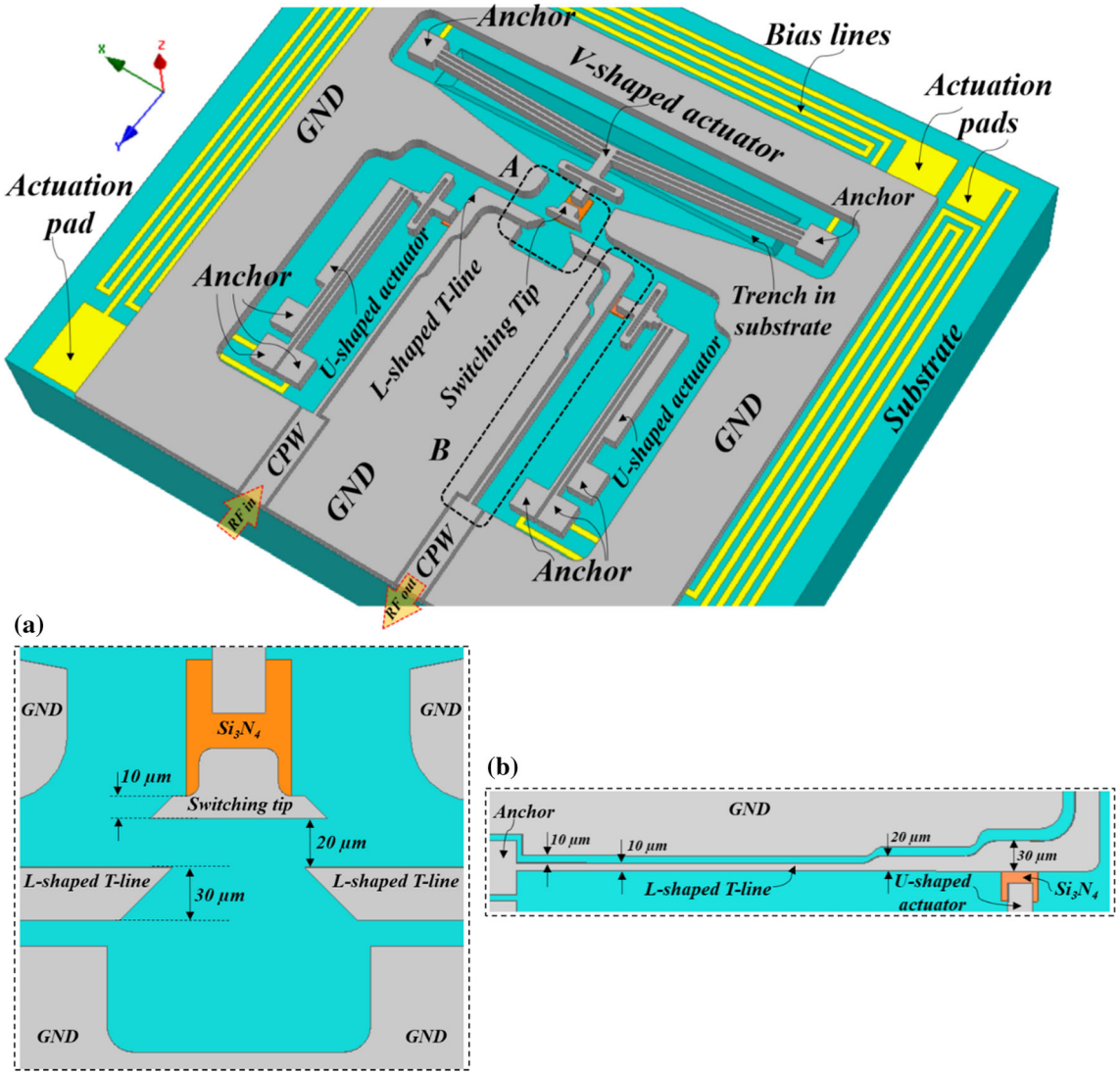

Fig. 1 A 3-D schematic view of the proposed switch and its different parts

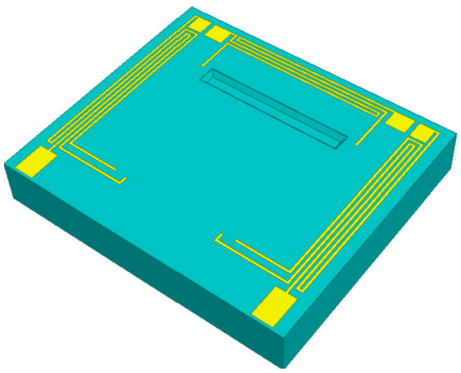

Fig. 2 Configuration of bias lines of the V-shaped and U-shaped actuators

2.2.2 Unlatching process (switch becomes OFF)

The unlatching process of the switch is schematically shown in Fig. 4 and is outlines here. (a) First, the V-shaped actuator is actuated in order to push the shuttle forward and break any unwanted connections as the result of micro-welding between switching tip and L-shaped T-lines. (b) Then, U-shaped actuators become activated to pull the L-shaped T-line backward and open the way for switching tip to come back to its rest position. (c) After that, the V-shaped actuator becomes OFF and switching tip goes back to its rest position. (d) Finally, the U-shaped actuators become OFF and switch becomes unlatched.

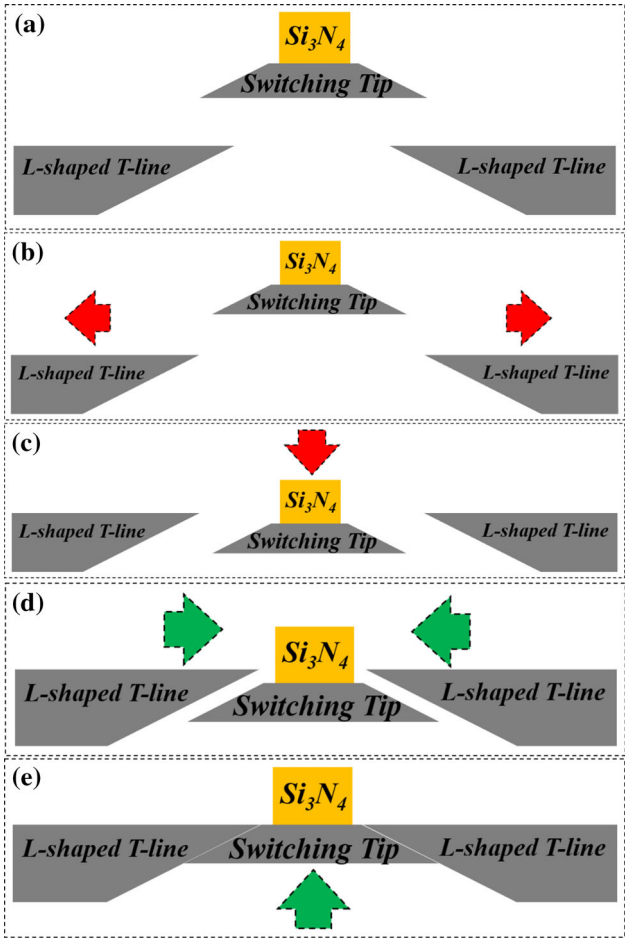

Fig. 3 Process of latching when the switch becomes ON. **a** Switch is normally OFF. **b** U-shaped actuators pull the L-shaped T-lines away from the switching tip. **c** V-shaped actuator pushes the switching tip forward. **d** U-shaped actuator becomes OFF and L-shaped T-lines come to their rest position. **e** V-shaped actuator becomes OFF and switching tip touches L-shaped T-lines and switch becomes ON

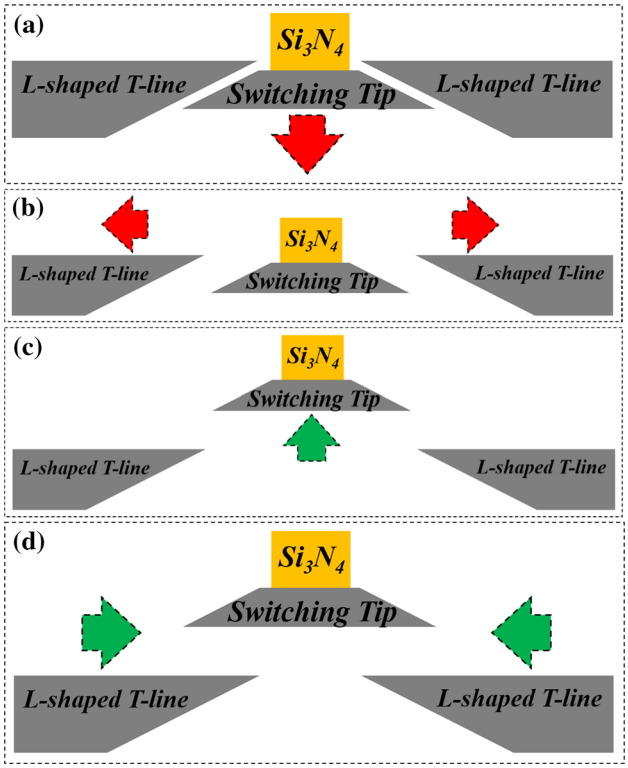

Fig. 4 The unlatching process of the switch. **a** V-shaped actuator is activated, **b** U-shaped actuators are activated to push L-shaped T-lines backward. **c** The V-shaped actuator becomes OFF and switching tip goes back to its rest position. **d** The U-shaped actuators become OFF and the L-shaped T-lines go back to their rest position

2.3 Proposed fabrication process

The standard MetalMUMPs process is adopted for fabrication of the switch. The step by step fabrication process is depicted in Fig. 5 and is outlines here. In proposed fabrication process flow, (a) 2 µm-thick oxide was first grown over a high resistivity silicon wafer. Then, a 0.5 µm-thick sacrificial phosphor silicate glass (PSG) layer was deposited as Oxide 1 layer. By the use of wet chemical etching, the unwanted sacrificial PSG was removed. Also, Oxide 1 layer is used to define the regions at which the silicon trench will be formed. (b) In order to isolate switch contact tip from the shuttle of the V-shaped actuator and at the same time provide strong mechanical support, two 0.35 µm-thick layers of silicon nitride (Si_3N_4) were deposited. After that, (c) in order to remove Si_3N_4 from unwanted areas, RIE etching was. (d) A second PSG layer as a sacrificial layer (Oxide 2) with thickness of 1.1 µm was deposited and wet etched and a thin metal layer was deposited. In the next step, (e) the base layer for the plating was deposited (this layer is not shown in Fig. 5). The base layer consists of 500 nm of Cu and 50 nm of Ti. In order to provide a stencil for the electroplated metal layer a thick layer of photoresist was deposited and patterned over the wafer. (f) Then, nickel was electroplated by a thickness of 20 µm into the patterned photoresist. (g) The photoresist stencil was then chemically removed. (h) Electroplating was used for deposition of a 1–3 µm gold layer as sidewall metal in order to provide a low resistance contact. (i) After that, the PSG sacrificial layers (Oxides 1 and 2) and the oxide layer over the trench areas were removed by HF solution. (j) Finally, A 25 µm deep trench was created inside of the silicon substrate in the areas defined by Oxide 1 layer. The trench was created by a KOH silicon etch and objective of its creation is to substantially decrease heat leakage and power dissipation from microelectro-thermal actuators to the silicon substrate.

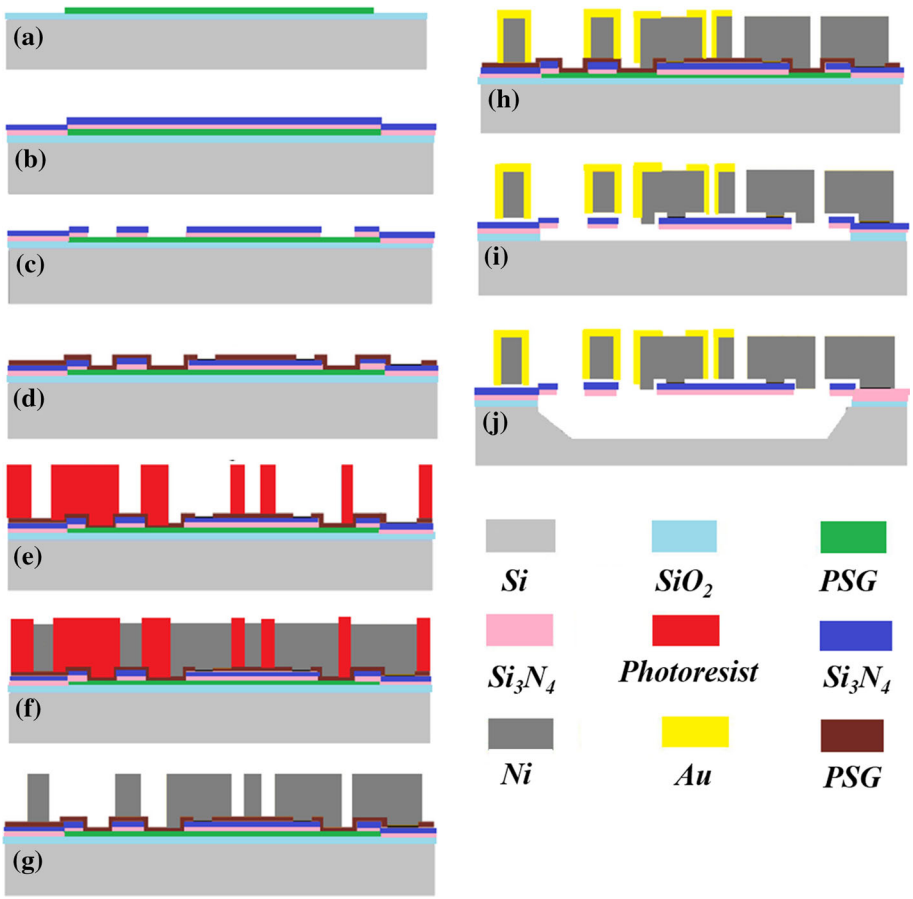

Fig. 5 Proposed fabrication process flow for the switch

3 Drive and latching actuators

Both U-shaped and V-shaped actuators are employed in the switch structure. The U-shaped microelectro-thermal actuators are used for latching and V-shaped actuator is used to drive the switching tip toward the L-shaped T-lines.

The U-shaped electro-thermal micro-actuators are very well documented in literatures (Bakri-Kassem and Mansour 2015; Phan et al. 2017; Shan et al. 2017; Zhang et al. 2017) and have numerous applications in RF MEMS devices and components (Daneshmand et al. 2009; Daneshmand and Mansour 2011; Ilkhechi et al. 2016a; Joshitha et al. 2017; Patel and Rebeiz 2012; Pirmoradi et al. 2015; Somà et al. 2017; Yan et al. 2003). The main advantages of these actuators are; large deflections, high produced forces, and low actuation voltages (Yan et al. 2003).

The latching part of the switch is done by two sets of identical U-shaped actuators. In order to understand operation, the operation mechanism of the U-shaped actuators are discussed here based on the Fig. 6.

By applying a DC voltage to actuation pads, as shown in Fig. 6, electrical current passes through the two narrow arms L_{H1} and L_{H2} (called hot arms). The large current density in hot arms causes them to heat up and create lateral motion toward the cold arm as the result of mechanical elongation.

The thermal expansion of the hot arms can be expressed as below:

$$\Delta L = \alpha \int_0^L (T - T_s) dx \tag{1}$$

where α is coefficient of thermal expansion of the nickel, L is the original length of the hot arms, and T is the temperature distribution over the hot arm (Yan et al. 2003). The heat flow equation can be derived by considering a differential element of the hot arm of thickness t, width W_H and length dx (Huang and Lee 1999). By considering the steady-state conditions for the heat transfer flow, the power generated as the result of resistive heating in the element is equal to the heat conduction and convection out of the element, as below equation;

$$\left[-k_p w_h t \frac{dT}{dx}\right]_x + J^2 \rho w_h t dx = \left[-k_p w_h t \frac{dT}{dx}\right]_{x+dx} + \frac{S w_h (T - T_s) dx}{R_T} \tag{2}$$

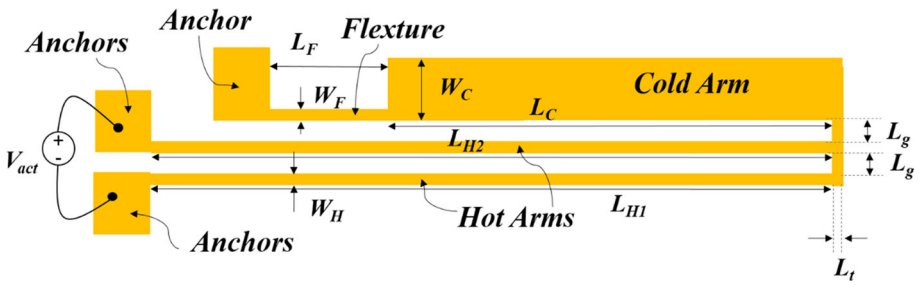

Fig. 6 A schematic view of the U-shaped elector-thermal micro-actuator

which k_p and ρ are nickel's thermal conductivity and resistivity, T and T_s are the hot arm and substrate's temperature, respectively; J is current density, and S is called the shape factor denoting the ratio of heat loss from the sides and bottom of the beam respect to the heat loss from the bottom of the beam only (Lin and Chiao 1996). If the hot arm is wide enough, the thermal resistance between the hot arm and the substrate is denoted by R_T (Huang and Lee 1999).

By taking the limit from Eq. (2) as $dx \to 0$, we have:

$$\frac{d^2T}{dx^2} = \frac{S(T - T_S)}{k_P R_T t} - \frac{J^2\rho}{k_p} \tag{3}$$

The resistivity ρ is dependent on the temperature of nickel. Here, the resistivity is written as;

$$\rho(T) = \rho_0[1 + \xi(T - T_s)] \tag{4}$$

At which ρ_0 is the resistivity of nickel in room temperature and ξ is a constant.

The current density is denoted by:

$$J = \frac{V}{\rho L} \tag{5}$$

where V is the applied voltage over the hot arms and L is the total length of the hot arm at which the electrical current passes through.

Substituting Eqs. (4) and (5) into Eq. (3) yields;

$$\frac{d^2T}{dx^2} = \frac{S(T - T_S)}{k_P R_T t} - \frac{V^2}{L^2 k_p \rho_0[1 + \xi(T - T_s)]} \tag{6}$$

The Taylor series expansion has been employed in order to linearize Eq. (6) and the result is;

$$\frac{d^2T}{dx^2} = \frac{S(T - T_S)}{k_P R_T t} - \frac{V^{2T - T_s}}{L^2 k_p \rho_0}[1 - \xi(T - T_s)] \tag{7}$$

Equation (7) is a linear differential equation and its solutions are;

$$T_{LH_1} = T_s + \frac{B_{LH_1}}{A^2_{LH_1}} + C_1 e^{A_{LH_1}x} + C_2 e^{-A_{LH_1}x} \tag{8}$$

$$B_{LH_1} = (V^2_{LH_1}/L^2_{LH_1} k_p \rho_0) \tag{8a}$$

$$A^2_{LH_1} = (S/k_P R_T t) + B_{LH_1}\xi \tag{8b}$$

$$T_{LH_2} = T_s + \frac{B_{LH_2}}{A^2_{LH_2}} + C_1' e^{A_{LH_2}x} + C_2' e^{-A_{LH_2}x} \tag{9}$$

$$B_{LH_2} = (V^2_{LH_2}/L^2_{LH_2} k_p \rho_0) \tag{9a}$$

$$A^2_{LH_2} = (S/k_P R_T t + B_{LH_2}\xi \tag{9b}$$

In Eqs. (8) and (9); C_1, C_2, C_1' and C_2' are obtained by the boundary conditions applied to the hot arms. V_{LH_1} and V_{LH_2} are the voltages over the hot arms of L_{H1} and L_{H2}.

When the thermal distribution over the hot arms is extracted, the thermal expansion can be formulated by Eq. (1) for both of the hot arms.

The deflection analysis of the microelectro-thermal actuator is documented in (Elms 1970; Navaratna 1965) using force method. According to virtual work method described in (Elms 1970), the deflection in the tip of the actuator can be calculated as:

$$u = \int_{L_{H1}} \frac{\bar{M}M}{EI_h} dx \tag{10}$$

where $\bar{M}$ is bending moment due to the virtual force, M is the bending moment of the hot arm due to the thermal expansion, E and I_h are the Young's modulus and the moment of the hot arm.

The dimensional parameters of the U-shaped actuators employed in switch structure are tabulated in Table 1.

The deflection of the actuator tip for various voltages is plotted in Fig. 7. Based on the deflection required for making the switch ON, the actuator needs a voltage of 0.5 V in order to generate a 12 μm deflection. Also, thermal distribution over the actuator for an actuation voltage of 0.5 V is plotted in Fig. 8 for analytical calculation and FEM simulation results. As apparent from the figure, there

Table 1 Dimensional parameters of the U-shaped actuator

Parameter	L_C	L_F	L_g	L_{H1}	L_{H2}	W_H	W_F	W_C	L_t
Value (μm)	320	100	15	500	500	10	10	50	10

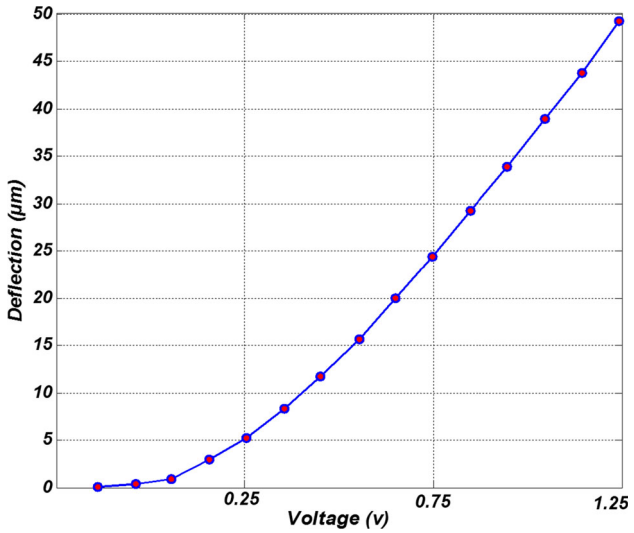

Fig. 7 Deflection of the U-shaped actuator for different actuation voltages. Based on the deflection required for making the switch ON, the actuator needs an actuation voltage of 0.5 V in order to generate a 12 μm deflection

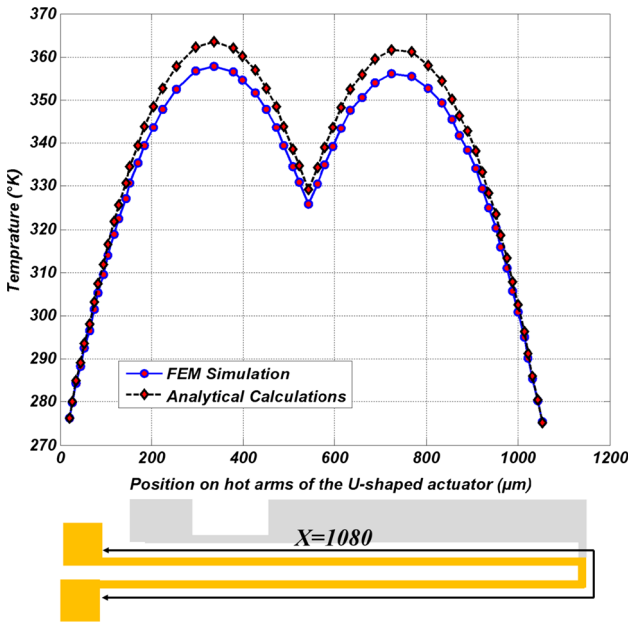

Fig. 8 FEM simulated and analytically calculated thermal distribution over the hot arms of U-shaped actuator for an actuation voltage of 0.5 V. As apparent from the figure, there is a good agreement between simulation and analytical model results

is a good agreement between analytical calculation and FEM simulation results and the maximum temperature over the structure is around 358 K. Also, the FEM simulation result for transient response of the U-shaped actuator for actuation voltage of 0.5 V is plotted in Fig. 9.

The power consumption of the U-shaped actuator for applied voltage of 0.5 V is about 0.625 W.

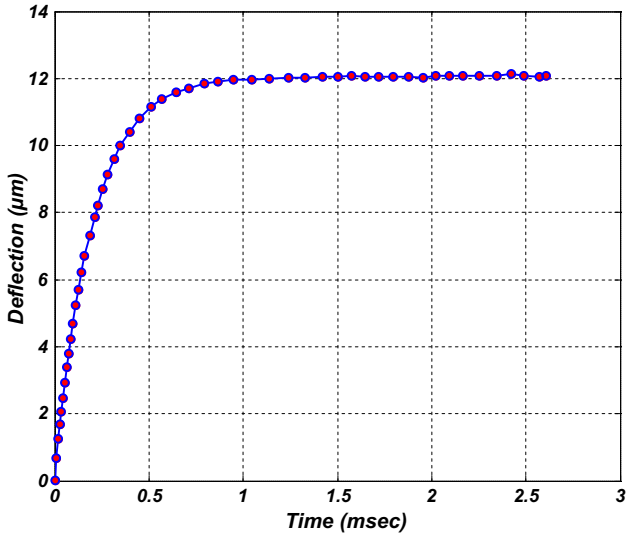

Fig. 9 The FEM simulation result for transient response of the U-shaped actuator for actuation voltage of 0.5 V

Similar to U-shaped microelectro-thermal actuators, V-shaped microelectro-thermal actuators are well-documented and have many applications in implementation of RF MEMS devices (Hassanpour et al. 2012; Shivhare et al. 2016; Zhang et al. 2013).

In the analysis of V-shaped actuator, for the sake of simplicity, the thermal conductivity, resistivity, and thermal expansion coefficient of the materials are initially assumed to be independent of temperature. Figure 10 displays the differential element of V-beam actuator applied the constant current for the model analysis. The steady-state heat equation can be written as (Maloney 2001)

$$k_n wh\frac{d^2T_{(x)}}{dx^2} + J^2\rho wh - Sk_a w\left(\frac{T_{(x)} - T_\infty}{g_a}\right) = 0 \tag{11}$$

where k_n is the thermal conductivity of nickel, k_a is the thermal conductivity of air, $T_{(x)}$ is the temperature on the position x of the beam, T_∞ is the ambient temperature, J is the current density through the beam, ρ is the resistivity of nickel, L is the length of V-beam between two anchors. Solving this differential equation with the boundary conditions, $T_{(0)} = T_{(L)} = T_\infty$, the temperature distribution on the V-beam is

$$T_{(x)} = T_\infty + \frac{J^2\rho}{k_n m^2}\left(1 - \frac{e^{m(L-x)} + e^{mx}}{e^{mL} + 1}\right) \tag{12}$$

where $m^2 = \frac{Sk_a}{k_n g_a h}$

The V-shaped beam will be buckled when the temperature rises because the beam is clamped at both ends and its total length is extended. The elastic deformation of the left half V-beam after Joule heating using the pseudo-rigid-body model is shown in Fig. 11. For the clamp-clamp beam, there is an inflection point in the middle of the

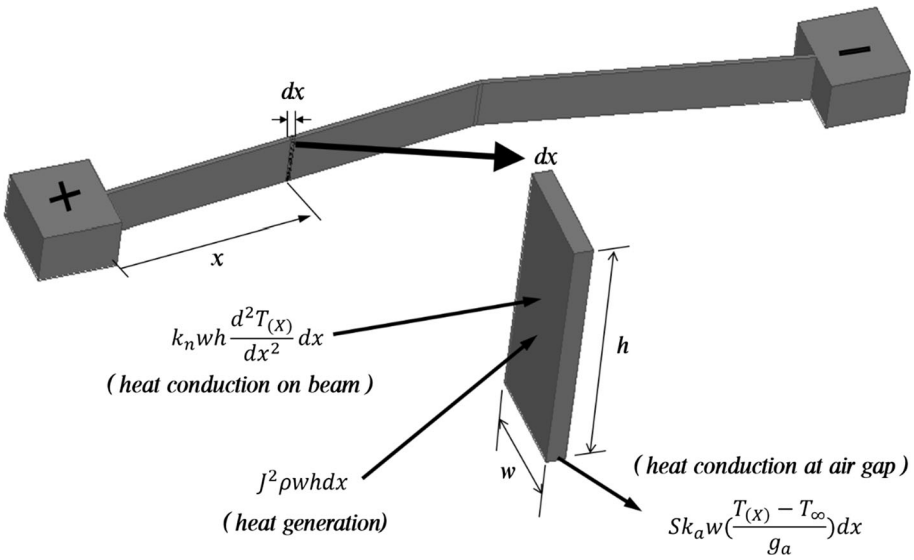

Fig. 10 Differential element of a V-shaped actuator used in the electro-thermal model analysis

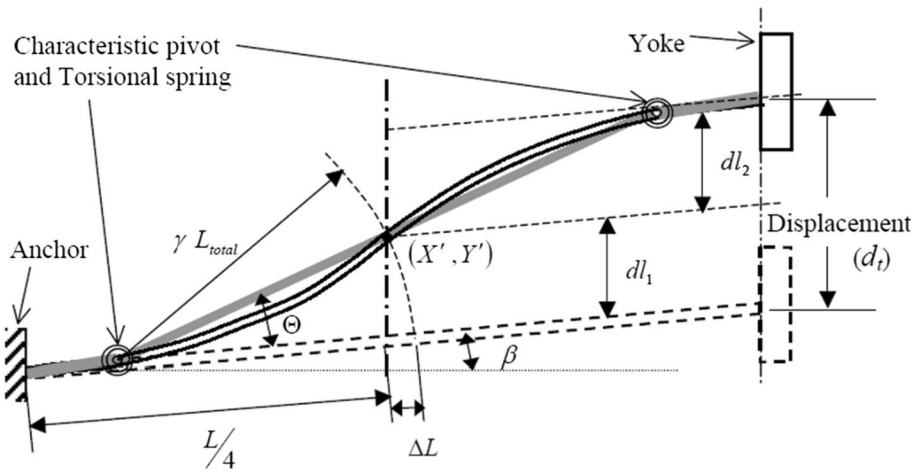

Fig. 11 Illustration of an elastic deformation of the left half V-beam using the pseudo-rigid-body model after Joule heating

deformed beam and only force without any moment applies at this point. It is reasonable that assuming this inflection point of the curve consistently resides in the middle place, and the displacement of thermal V-beam after Joule heating can be calculated as the following steps using this assumption. First, the total length of V-beam for the first quarter after thermal expansion, $L_{total,}$ is calculated by:

$$L_{total} = \frac{L}{4} + \Delta L = \frac{L}{4} + \alpha \int_0^{L/4} [T_{(x)} - T_\infty]dx = \frac{L}{4} + \frac{\alpha J^2 \rho}{k_n m^2}\left[\frac{L}{4} + \frac{\sinh(mL/4)}{m\cosh(mL/2)} - \frac{\tanh(mL/2)}{m}\right] \quad (13)$$

where α is a thermal expansion coefficient. Based on the pseudo-rigid-body model and the above assumption, the position of the inflection point (X′, Y′) can be obtained as

$$X' = \frac{L}{4}\cos(\beta) \quad (14)$$

$$Y' = \sqrt{\gamma^2 L_{total}^2 - \left(\frac{L}{4}\cos(\beta) - (1-\gamma)L_{total}\cos(\beta)\right)^2} + (1-\gamma)L_{total}\sin(\beta) \quad (\gamma = 0.8517) \quad (15)$$

where β is an offset angle of the thermal V-beam and γ is a characteristic radius factor in the pseudo-rigid-body model. Then, the deflection as the result of this quarter length, dl_1, is extracted by;

$$dl_1 = Y' - \frac{L}{4}\sin(\beta) \quad (16)$$

The temperature distribution is different between the first quarter and the second quarter of the V-beam. Hence, deflection of each quarter is necessary to consider

separately. The total length of thermal V-beam for the second quarter after thermal expansion, L'_{total}, is

$$L'_{total} = \frac{L}{4} + \alpha \int_{L/4}^{L/2} [T_{(x)} - T_\infty] dx = \frac{L}{4} + \frac{\alpha J^2 \rho}{k_n m^2} \left[\frac{L}{4} - \frac{\sinh(mL/4)}{m \cosh(mL/2)} \right] \quad (17)$$

Using the same calculations, the deflection created from second quarter length, dl_2, is

$$dl_2 = \sqrt{\gamma^2 L'^2_{total} - \left(\frac{L}{4} \cos(\beta) - (1-\gamma) L'_{total} \cos(\beta) \right)^2} + (1-\gamma) L'_{total} \sin(\beta) - \frac{L}{4} \sin(\beta) \quad (18)$$

Then, the total displacement of thermal V-beam, d_t, is the summation of dl_1 and dl_2, as follow;

$$d_t = dl_1 + dl_2 \quad (19)$$

The geometry and dimension of the V-shaped actuator employed in switch structure is plotted in Fig. 12.

Figure 13 shows deflection of the actuator's tip for different actuation voltages applied to the actuator. Based on this figure, an actuation voltage of 0.9 V is required in order to produce a deflection of about 32 µm. The thermal distribution over the V-shaped structure for actuation voltage of 0.9 V for FEM simulations and analytical calculations are shown in Fig. 14. As shown in the figure, there is a good agreement between FEM simulations and analytical calculations and the maximum temperature over the actuator beams reaches around 452 K. The V-shaped structure consumes a power of 0.56 W for the applied voltage of 0.9 V. The FEM simulation result for transient response of the actuator is also plotted in Fig. 15.

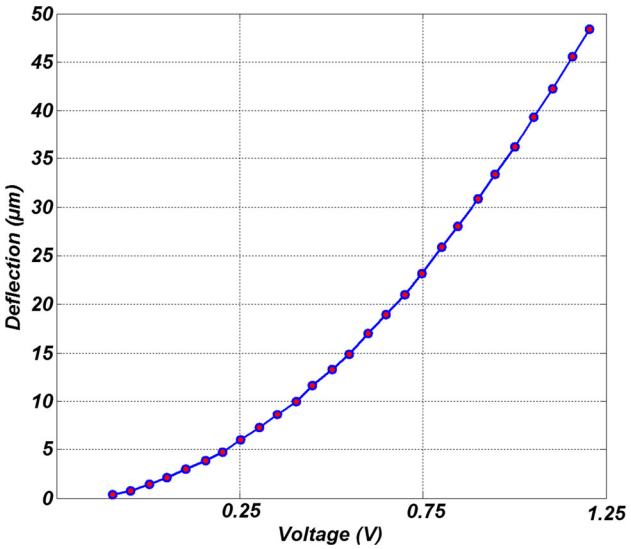

Fig. 13 Generated deflection of the V-shaped actuator respect to applied voltage

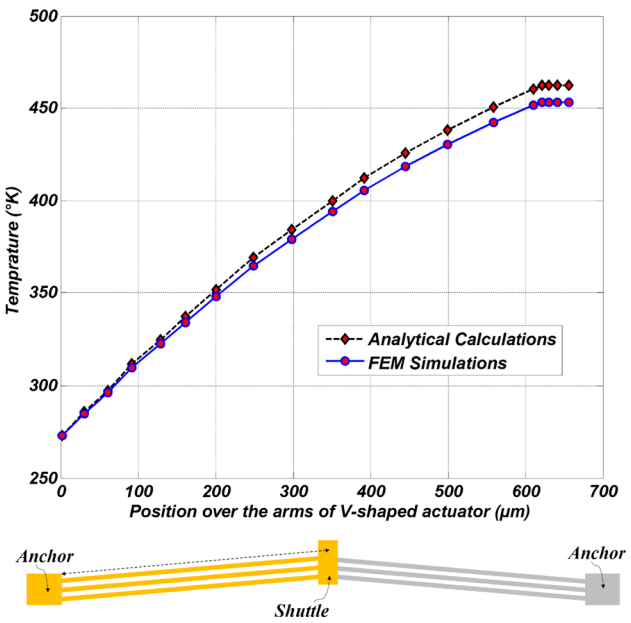

Fig. 14 Analytically calculated and simulated results for thermal distribution over half side of the V-shaped actuator. Because the thermal distribution over the beams of the actuator are symmetric, half-sided results are provided. As apparent from the figure, there is a good agreement between the results

4 Results and discussion

4.1 RF results

4.1.1 RF design

In this design in order to have an excellent RF performance, a step by step process is followed from designing and improving a co-planar waveguide (CPW) T-line characteristics to the final structure of the switch. The step by step process is outlines in Fig. 16. (a) In the first step, a CPW line is designed and its width, length and gap to the GND are optimized to attain the

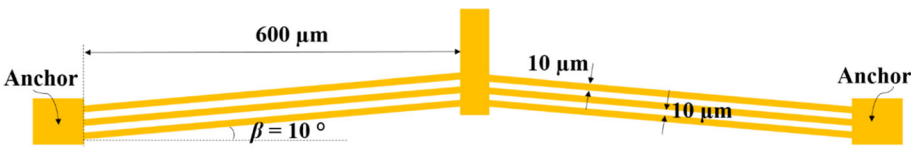

Fig. 12 Structure and dimensions of the V-shaped microelectro-thermal actuator employed in switch structure

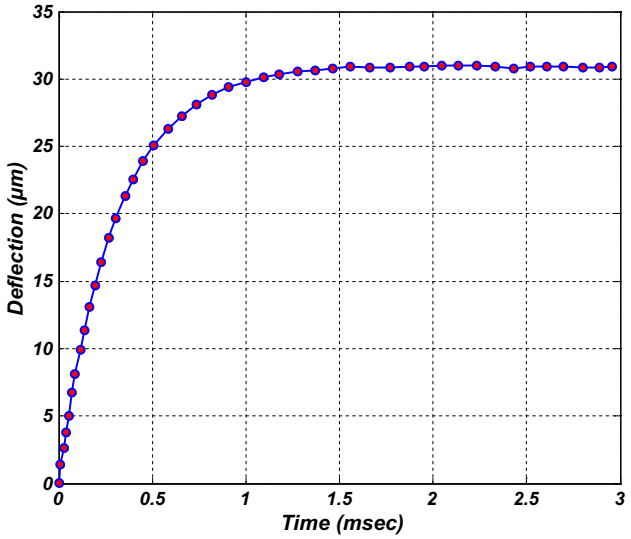

Fig. 15 The FEM simulation result for transient response of the V-shaped actuator for actuation voltage of 0.9 V

best dimensions with low loss. (b) Then, the location for switching tip and V-shaped thermal actuator was emptied inside of the GND line. (c) After that, the location for U-shaped actuators was created inside of the GND. (d) Finally, the U-shaped and V-shaped actuators were embedded inside of the switch. The variations of insertion loss and return loss after each step is plotted in Fig. 17.

The RF performance of the switch including return loss, insertion loss and isolation are summarized in Fig. 18 up to 150 GHz. Based on this figure, the return loss is below − 10 dB up to 100 GHz, insertion loss is below − 0.1 dB up to 40 GHz, and isolation is better than − 20 dB up to 100 GHz.

4.2 Mechanical results

4.2.1 Contact resistance

Because of roughness of contact areas between switch and T-line, there is a finite resistance in the contact points

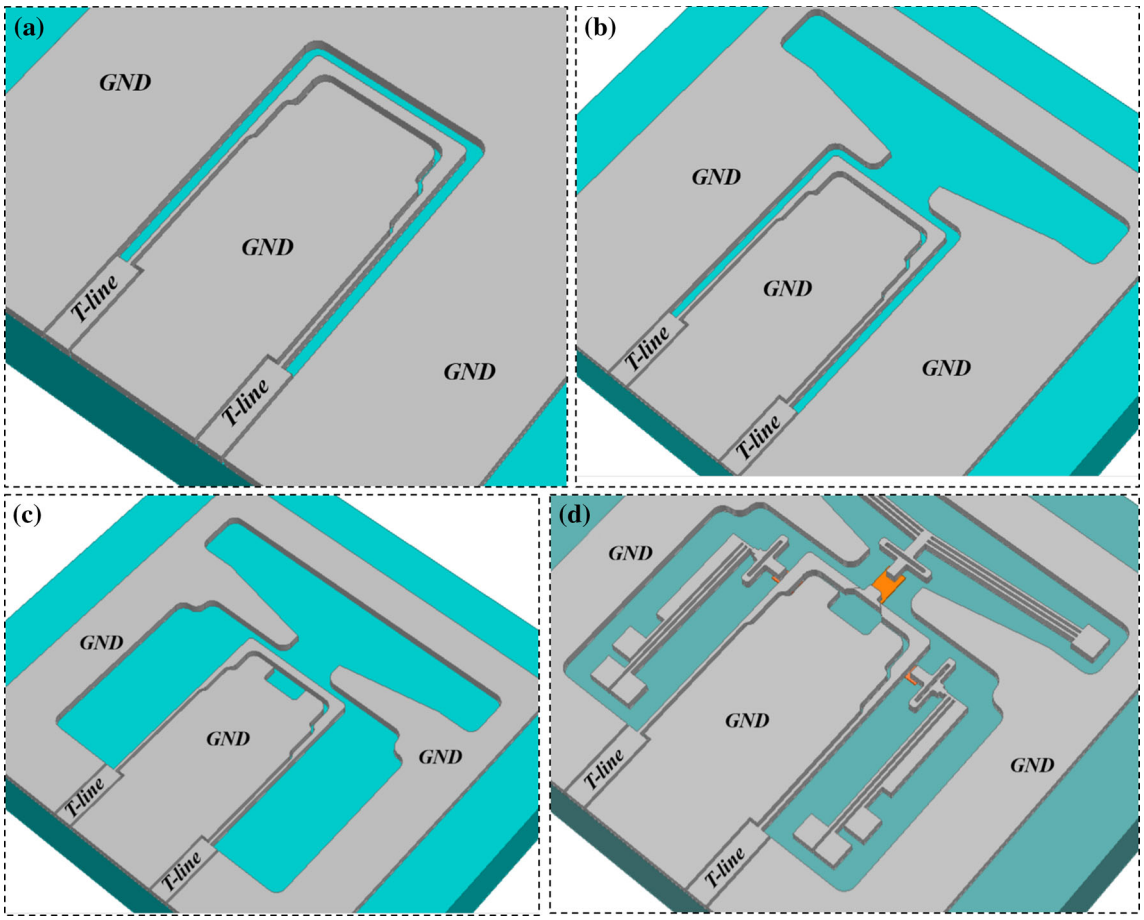

Fig. 16 RF design procedure of the switch. **a** The CPW T-line is design. **b** The location of V-shaped actuator is emptied inside of the GND. **c** The location of U-shaped actuators are created inside of the GND. **d** The U-shaped and V-shaped actuators and switching tip are integrated inside of the switch

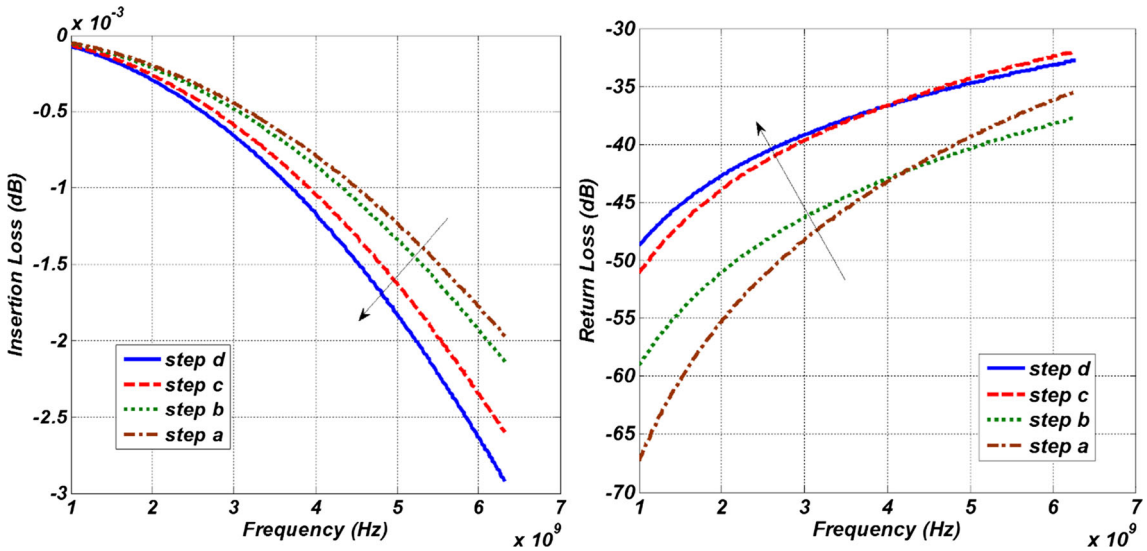

Fig. 17 Insertion loss and return loss variations for different steps outlined in RF design procedure

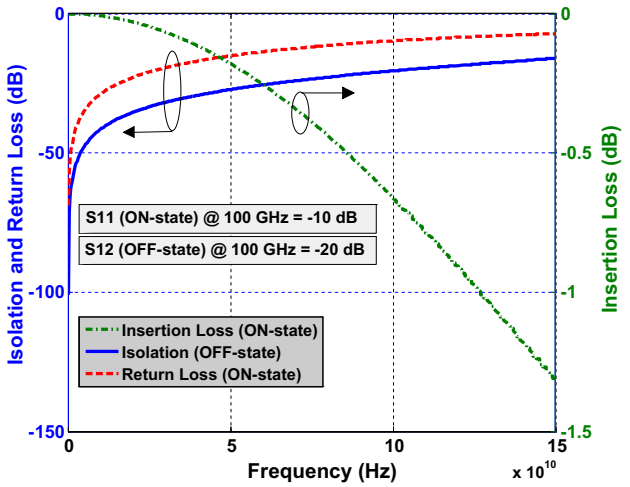

Fig. 18 RF performance of the switch including return loss, insertion loss, and isolation

(Bakri-Kassem and Mansour 2015; Daneshmand and Mansour 2011; Patel and Rebeiz 2010). This phenomena is dominant for DC-contact RF MEMS switches.

In the proposed switch here, based on Fig. 1, when the switch becomes ON, there will be a finite resistance between L-shaped T-lines and switching tip. The contact resistance degrades the insertion loss of the switch. Commercially available high frequency simulation tools (like HFSS®) do NOT consider the contact resistance (Bakri-Kassem and Mansour 2015; Mirzajani et al. 2014). In simulations, the contact materials are perfectly connected to each other. Hence, the contact resistance need to be extracted separately.

The contact resistance can be expressed by (Mastrangeli et al. 2006);

Table 2 MetalMUMPs electroplated nickel material properties

Description	Unit	Value
Electrical resistivity	Ω m	8×10^{-8}
Coefficient of thermal resistance	Ω	4×10^{-3}
Thermal conductivity	W m^{-1} K^{-1}	90.5
Specific heat capacity	J kg^{-1} K^{-1}	440
Coefficient of thermal expansion	K^{-1}	6.41×10^{-3}
Density	kg m^{-3}	8900
Young's modulus	GPa	159

$$R_c = \frac{\rho}{2a} + R_r \tag{20}$$

$$a = \sqrt{\frac{F_c}{\pi H}} \tag{21}$$

At which, ρ is the resistivity of the contact material, R_r is an additional resistance due to resistive contamination, H is the Meyer indentation hardness of contact material [1.6 GPa for Au (Wu et al. 2005)], and F_c is the contact force. Maxwell spreading resistance and Sharvin resistance, do not qualitatively effect the analysis (Matsuda 2011).

In the Eq. (21), the contact force (F_c) can be estimated by the following equation:

$$F_c = \sigma \times A \tag{22}$$

At which σ is the mechanical stress at contact area, F_c is contact force and A is the area of contact.

Based on FEM simulations, the mechanical stress on the contact area is calculated to be about 3.3×10^6 N m^{-2} [well below the yield stress of the nickel (Fritz et al. 2002)], also the contact area (A) is around

Table 3 Comparing operating parameters of the proposed switch with previous works

	(Deng et al. 2017)	(Molaei and Ganji 2017)	(Zhu et al. 2013)	(Li et al. 2017b)	(Demirel et al. 2017)	(Ilkhechi et al. 2017)	This work
Voltage (V)	83	2.9	0.55	20	29	50	0.5–0.9
Insertion loss (dB)	− 0.15	− 1.01	− 0.5	− 0.35	− 0.4	− 0.87	− 0.1
Isolation (dB)	− 25	− 55	− 22.5	− 35	− 35	− 35	− 30
Power consumption (W)	NZ[a]	NZ[a]	2.11[b]	NZ[a]	NZ[a]	NZ[a]	NZ[a]

[a]Near Zero

[b]Estimated

20 μm × 14.14 μm. The contact force (F_c) can be calculated by Eq. (22) and is 0.95 mN. By substituting the parameters in Eqs. (20) and (21), the contact resistance is calculated for each contact and is 0.028 Ω. The overall contact resistance at which signal experiences while passing through the switch is about 0.06736 Ω.

The material properties used for FEM simulation of the switch is provided in Table 2.

In summary, the U-shaped actuators require an actuation voltage of about 0.5 V in order to produce 12 μm deflection for the L-shaped T-lines. This actuation voltage leads to a power consumption of about 0.625 W. The V-shaped actuator needs an actuation voltage of 0.9 V in order to push the switching tip 32 μm forward. The power consumption is about 0.56 mW. The maximum thermal distribution for U-shaped and V-shaped actuators is 358 and 452 K, respectively. Because of a 30 μm residual deflection stored in V-shaped actuator at the ON-state of the switch, the contact force between L-shaped T-lines and switching tip is 0.95 mN leading to a contact resistance of 0.028 Ω.

In order to bring out the functionality of the proposed switch, Table 3 compares the operation characteristics of proposed switch in this paper with previously published ones.

Based on the data presented in comparison table, the proposed switch has merits on lower actuation voltage, lower insertion loss and higher isolation respect to some of the recently published works.

5 Conclusion

In this paper, a new RF MEMS switch is designed for low loss and low power consumption applications. Micro-electro-thermal actuators are employed in switch structure in order to enhance the contact force and consequently decrease the contact resistance of the switch. Thanks to latching mechanism embedded in the switch structure, DC power consumption of the switch is confined to the transition time between OFF and ON states. The mechanical design of the switch is in such a way that, the contact force of the switch is very high without consuming any DC power. The switch works with low voltage ranges of 0.5 and 0.9 V for U-shaped and V-shaped actuators, respectively. The contact force and contact resistance of the switch are also investigated and based on analytical and numerical simulations, the contact resistance is 0.028 Ω. The insertion loss of the switch is better than − 0.1 dB up to 40 GHz, return loss is below − 10 dB up to 100 GHz and isolation is better than − 40 dB up to 100 GHz. The proposed switch in this paper is dedicated for applications in mobile front-ends especially antenna switch networks where the signal loss and power consumption are the main constraints.

Acknowledgements The authors are very grateful to Dr. Habib Badri Ghavifekr for his fruitful discussions and technical assistance on this project.

Compliance with ethical standards

Conflict of interest The authors declare no conflict of interest.

References

Atashzaban E, Mirzajani H, Nasiri M, Sangsefidi M (2013a) A large stroke MEMS-based linear motor for fourier transform spectrometer applications. Sens Transducers 151:47

Atashzaban E, Nasiri M, Mirzajani H, Demaghsi H, Ghavifekr HB (2013b) Design and simulation of a MEMS-based large traveling linear motor for near infrared fourier transform spectrometer. Sens Transducers 151:41

Bakri-Kassem M, Mansour RR (2015) High power latching RF MEMS switches. IEEE Trans Microw Theory Tech 63:222–232

Barzegar S, Mirzajani H, Ghavifekr HB (2015) A new linearly tunable RF MEMS varactor with latching mechanism for low voltage and low power reconfigurable networks. Wireless Pers Commun 83:2249–2265

Bian H, Shan C, Chen F, Yang Q, Li Y, Li Q (2017) Miniaturized 3-D solenoid-type micro-heaters in coordination with 3-D microfluidics. J Microelectromech Syst 26:588–592

Bonthu M, Sharma AK (2017) An investigation of dielectric material selection of RF-MEMS switches using Ashby's methodology for RF applications Microsyst Technol. https://doi.org/10.1007/s00542-017-3539-x

Chan KY, Daneshmand M, Mansour RR, Ramer R (2009) Scalable RF MEMS switch matrices: methodology and design. IEEE Trans Microw Theory Tech 57:1612–1621

Cheng Y, Zhang W, Tang J, Sun D, Chen W (2015) A MEMS piezoelectric solid disk gyroscope with improved sensitivity. Microsyst Technol 21(6):1371–1377

Cowen A et al (2002) MetalMUMPs design handbook MEMSCAP revision 1

Daneshmand M, Mansour R (2011) RF MEMS satellite switch matrices. IEEE Microw Mag 12:92–109

Daneshmand M, Fouladi S, Mansour RR, Lisi M, Stajcer T (2009) Thermally actuated latching RF MEMS switch and its characteristics. IEEE Trans Microw Theory Tech 57:3229–3238

Demaghsi H, Mirzajani H, Atashzaban E, Ghavifekr HB (2012) Design and simulation of a microgripper with the ability of releasing nano particles by vibrating end-effectors. Sens Transducers 144(9):131

Demaghsi H, Mirzajani H, Ghavifekr HB (2014a) A novel electrostatic based microgripper (cellgripper) integrated with contact sensor and equipped with vibrating system to release particles actively. Microsyst Technol 20(12):2191–2202

Demaghsi H, Mirzajani H, Ghavifekr HB (2014b) Design and simulation of a novel metallic microgripper using vibration to release nano objects actively. Microsyst Technol 20(1):65–72

Demirel K, Yazgan E, Demir Ş, Akın T (2017) A folded leg Ka-band RF MEMS shunt switch with amorphous silicon (a-Si) sacrificial layer. Microsyst Technol 23:1191–1200

Deng P, Wang N, Cai F et al (2017) A high-force and high isolation metal-contact RF MEMS switch. Microsyst Technol 23:4699. https://doi.org/10.1007/s00542-017-3302-3

Driesen M, Ceyssens F, Decoster J, Puers R (2010) Nickel-plated thermal switch with electrostatic latch. Sens Actuators A 164:148–153

Elms D (1970) Linear elastic analysis. Batsford, London

Fritz T, Cho H, Hemker K, Mokwa W, Schnakenberg U (2002) Characterization of electroplated nickel. Microsyst Technol 9:87–91

Hassanpour PA, Nieva PM, Khajepour A (2012) A passive mechanism for thermal stress regulation in micro-machined beam-type structures. Microsyst Technol 18:543–556

He X, Lv Z, Liu B, Li Z (2012) High-isolation lateral RF MEMS capacitive switch based on HfO 2 dielectric for high frequency applications. Sens Actuators A 188:342–348

Huang Q-A, Lee NKS (1999) Analysis and design of polysilicon thermal flexure actuator. J Micromech Microeng 9:64

Ilkhechi AK, Mirzajani H, Aghdam EN, Ghavifekr HB (2016a) A new electrothermally actuated 3-state high isolation and low power RF MEMS switch with latching mechanism. In: IEEE 2016 24th Iranian conference on electrical engineering (ICEE), pp 1634–1639. https://doi.org/10.1109/IranianCEE.2016.7585783

Ilkhechi AK, Mirzajani H, Aghdam EN, Ghavifekr HB (2016b) A novel SPDT rotary RF MEMS switch for low loss and power efficient signal routing. IETE J Res 62(1):68–80

Ilkhechi AK, Mirzajani H, Aghdam EN et al (2017) A new electrostatically actuated rotary three-state DC-contact RF MEMS switch for antenna switch applications. Microsyst Technol 23:231. https://doi.org/10.1007/s00542-015-2714-1

Ivanoff CS et al (2016) AC electrokinetic drug delivery in dentistry using an interdigitated electrode assembly powered by inductive coupling. Biomed Microdevice 18:84

Jain V, Raj TP, Deshmukh R, Patrikar R (2017) Design, fabrication and characterization of low cost printed circuit board based EWOD device for digital microfluidics applications. Microsyst Technol 23:389–397

Jayanthi VSPKSA, Das AB, Saxena U (2016) Recent advances in biosensor development for the detection of cancer biomarkers. Biosens Bioelectron 91:15–23. https://doi.org/10.1016/j.bios.2016.12.014

Joshitha C, Sreeja B, Princy SS, Radha S (2017) Fabrication and investigation of low actuation voltage curved beam bistable MEMS switch. Microsyst Technol 23:4553–4566

Kahmen G, Schumacher H (2017) Interactive design of MEMS varactors with high accuracy and application in an ultralow noise MEMS-based RF VCO. IEEE Trans Microw Theory Tech 65(10):3578–3584

Kumar N, Singh YK (2017) RF-MEMS-based bandpass-to-bandstop switchable single-and dual-band filters with variable FBW and reconfigurable selectivity. IEEE Trans Microw Theory Tech 65(10):3824–3837. https://doi.org/10.1109/TMTT.2017.2696004

Lakshmipriya T, Gopinath SCB, Hashim U (2017) Influenza viral detection on microfluidic delivery assisted biosensors. Microsyst Technol. https://doi.org/10.1007/s00542-017-3555-x

Li H, Chen J, Zhang J, Zhang N, Wang L, Zheng J (2017a) Freestanding electrostatic scratch drive microstructures using lamination of photosensitive films for microfluidics and microrobotics applications. Microsyst Technol 1–6

Li M, Zhao J, You Z, Zhao G (2017b) Design and experimental validation of a restoring force enhanced RF MEMS capacitive switch with stiction-recovery electrodes. Microsyst Technol 23:3091–3096

Lin L, Chiao M (1996) Electrothermal responses of lineshape microstructures. Sens Actuators A 55:35–41

Liu Y, Bey Y, Liu X (2017) High-power high-isolation RF-MEMS switches with enhanced hot-switching reliability using a shunt protection technique. IEEE Trans Microw Theory Tech 65(9):3188–3199. https://doi.org/10.1109/TMTT.2017.2687427

Lu Q, Bai J, Wang K, He S (2017) Design, optimization, and realization of a high-performance MOEMS accelerometer from a double-device-layer SOI wafer. J Microelectromech Syst 26(4):859–869. https://doi.org/10.1109/JMEMS.2017.2693341

Lucibello A, Marcelli R, Di Paola E et al (2017) Fabrication and test of RF MEMS in LTCC technology. Microsyst Technol. https://doi.org/10.1007/s00542-017-3419-4

Maloney JM (2001) Fabrication and thermal actuation of 3-D micro electro mechanical systems Master's thesis. University of Maryland, College Park

Mastrangeli M, Nannini A, Paci D, Pieri F (2006) Equivalent circuit for RF flexural free–free MEMS resonators. J Comput Electron 5:205–210

Matsuda K (2011) Equivalent-circuit model for electrostatic microtorsion mirror. J Comput Electron 10:136–140

Mirzajani H, Pourmand A, Aghdam EN, Ghavifekr HB (2014) Frequency agile MEMS patch antenna for reconfigurable RF front-ends. In: IEEE 2014 22nd Iranian conference on electrical engineering (ICEE), pp 393–398. https://doi.org/10.1109/IranianCEE.2014.6999571

Mirzajani H, Ghavifekr HB, Aghdam EN, Demaghsi H, Vafaie RH (2015) Enhancement of mechanical resonant modes by miniaturization of frequency tunable MEMS-enabled microstrip patch antenna. Microsyst Technol 21:773–783

Mirzajani H, Cheng C, Wu J, Ivanoff CS, Aghdam EN, Ghavifekr HB (2016) Design and characterization of a passive, disposable wireless AC-electroosmotic lab-on-a-film for particle and fluid manipulation. Sens Actuators B Chem 235:330–342

Mirzajani H, Aghdam EN, Ghavifekr HB, Jafarpour A (2017a) 3-state, high contact and release force RF MEMS switch designed based on MetalMUMPs process. In: IEEE 2017 Iranian conference on electrical engineering (ICEE), pp 318–323. https://doi.org/10.1109/IranianCEE.2017.7985463

Mirzajani H, Cheng C, Wu J, Chen J, Eda S, Aghdam EN, Ghavifekr HB (2017b) A highly sensitive and specific capacitive aptasensor for rapid and label-free trace analysis of Bisphenol A (BPA) in canned foods. Biosens Bioelectron 89:1059–1067

Mirzajani H, Ilkhechi AK, Zolfaghari P, Azadbakht M, Aghdam EN, Ghavifekr HB (2017c) Power efficient, low loss and ultra-high isolation RF MEMS switch dedicated for antenna switch applications. Microelectron J 69:64–72

Molaei S, Ganji BA (2017) Design and simulation of a novel RF MEMS shunt capacitive switch with low actuation voltage and high isolation. Microsyst Technol 23:1907–1912

Navaratna R (1965) Application of matrix displacement method to linear elastic analysis of shells of revolution. AIAA J 3(11):2138–2145. https://doi.org/10.2514/3.3326

Muldavin J, Bozler C, Wyatt P (2012) Stiction in RFMEMS capacitive switches. In: 2012 IEEE MTT-S international microwave symposium digest (MTT), pp 1–3

Nouet P, Michel B (2017) Special issue on design, test, integration and packaging of MEMS and MOEMS (DTIP 2015), held in Montpellier, France, April 27–30, 2015. Springer

Okyay AK et al (2017) Using nanogap in label-free impedance based electrical biosensors to overcome electrical double layer effect. Microsyst Technol 23:889–897

Patel CD, Rebeiz GM (2010) An RF-MEMS switch with mN contact forces. In: IEEE 2010 microwave symposium digest (MTT), MTT-S International, pp 1242–1245

Patel CD, Rebeiz GM (2012) A high-reliability high-linearity high-power RF MEMS metal-contact switch for DC-40-GHz applications. IEEE Trans Microw Theory Tech 60:3096–3112

Phan HP, Nguyen MN, Nguyen NV, Chu DT (2017) Analytical modeling of a silicon-polymer electrothermal microactuator. Microsyst Technol 23:101–111

Pirmoradi E, Mirzajani H, Ghavifekr HB (2015) Design and simulation of a novel electro-thermally actuated lateral RF MEMS latching switch for low power applications. Microsyst Technol 21:465–475

Proie RM, Ivanov T, Pulskamp JS, Polcawich RG (2012) A compact, low loss piezoelectric RF MEMS relay with sub 100-ns switching times. In: IEEE microwave symposium digest (MTT), MTT-S International, pp 1–3

Rebeiz GM (2004) RF MEMS: theory, design, and technology. Wiley, New York

Rebeiz GM, Entesari K, Reines IC, Park S-J, El-Tanani MA, Grichener A, Brown AR (2009) Tuning into RF MEMS. IEEE Microw Mag 10:55–72

Rebeiz GM, Patel CD, Han SK, Ko C-H, Ho KM (2013) The search for a reliable MEMS switch. IEEE Microw Mag 14:57–67

Shan T, Qi X, Cui L, Zhou X (2017) Thermal behavior modeling and characteristics analysis of electrothermal microactuators. Microsyst Technol 23:2629–2640

Shivhare P, Uma G, Umapathy M (2016) Design enhancement of a chevron electrothermally actuated microgripper for improved gripping performance. Microsyst Technol 22:2623–2631

Somà A, Iamoni S, Voicu R et al (2017) Design and experimental testing of an electro-thermal microgripper for cell manipulation. Microsyst Technol. https://doi.org/10.1007/s00542-017-3460-3

Song Y-H, Gong S (2017) Wideband spurious-free lithium niobate RF-MEMS filters. J Microelectromech Syst 26(4):820–828. https://doi.org/10.1109/JMEMS.2017.2671445

Sterner M, Roxhed N, Stemme G, Oberhammer J (2011) Electrochemically assisted maskless selective removal of metal layers for three-dimensional micromachined SOI RF MEMS transmission lines and devices. J Microelectromech Syst 20:899–908

Takalkar S, Baryeh K, Liu G (2017) Fluorescent carbon nanoparticle-based lateral flow biosensor for ultrasensitive detection of DNA. Biosens Bioelectron 98:147–154

Tingkai Z, Chaoyang X, Ling Z, Wei W (2015) Study on a vibratory tri-axis MEMS gyroscope with single drive and multiple axes angular rate sense. Microsyst Technol 21(10):2145–2154

Trigona C, Andò B, Baglio S (2016) Fabrication and characterization of an MOEMS gyroscope based on photonic bandgap materials. IEEE Trans Instrum Meas 65:2840–2852

Vafaie RH, Mahdipour M, Mirzajani H, Ghavifekr HB (2013) Numerical simulation of mixing process in tortuous microchannel. Sens Transducers 151(4):30

Wang Y-H, Huang K-J, Wu X (2017) Recent advances in transition-metal dichalcogenides based electrochemical biosensors: a review. Biosens Bioelectron 97:305–316. https://doi.org/10.1016/j.bios.2017.06.011

Wu J, Quinn V, Bernstein GH (2005) An inductive link with integrated receiving coil—coupling coefficient and link efficiency. J Comput Electron 4:221–230

Xiang H, Shi Z (2009) Static analysis for functionally graded piezoelectric actuators or sensors under a combined electro-thermal load. Eur J Mech A Solids 28:338–346

Xu Y, Liu S, Wang S (2017) Miniaturized two-dimensional optical scanner based on planar waveguide and flexible printed circuit beam deflectors. IEEE Photonics J 9:1–11

Yan D, Khajepour A, Mansour R (2003) Modeling of two-hot-arm horizontal thermal actuator. J Micromech Microeng 13:312

Yıldırım E (2017) Analysis and testing of a contraction-and-expansion micromixer for micromilled microfluidics Microsyst Technol 23:4797. https://doi.org/10.1007/s00542-017-3291-2

Zhang R, Chu J, Wang H, Chen Z (2013) A multipurpose electrothermal microgripper for biological micro-manipulation. Microsyst Technol 19:89–97

Zhang Z, Yu Y, Liu X, Zhang X (2017) Dynamic modelling and analysis of V-and Z-shaped electrothermal microactuators. Microsyst Technol 23:3775–3789

Zhu Y-Q, Han L, Wang L-F, Tang J-Y, Huang Q-A (2013) A novel three-state RF MEMS switch for ultrabroadband (DC-40 GHz) applications. IEEE Electron Device Lett 34:1062–1064